

Dipole excited states in ^{11}Li with complex scaling

E. Garrido

Instituto de Estructura de la Materia, CSIC, Serrano 123, E-28006 Madrid, Spain

D.V. Fedorov and A.S. Jensen

Institute of Physics and Astronomy, Aarhus University, DK-8000 Aarhus C, Denmark

Abstract

The 1^- excitations of the three-body halo nucleus ^{11}Li are investigated. We use adiabatic hyperspherical expansion and solve the Faddeev equations in coordinate space. The method of complex scaling is used to compute the resonance states. The Pauli forbidden states occupied by core neutrons are excluded by constructing corresponding complex scaled phase equivalent two-body potentials. We use a recently derived neutron-core interaction consistent with known structure and reaction properties of ^{10}Li and ^{11}Li . The computed dipole excited states with $J^\pi = 1/2^+$, $J^\pi = 3/2^+$, and $J^\pi = 5/2^+$ have energies ranging from 0.6 MeV to 1.0 MeV and widths between 0.15 MeV and 0.65 MeV. We investigate the dependence of the complex energies of these states on the ^{10}Li spectrum. The finite spin $3/2$ of the core and the resulting core-neutron spin-spin interaction are important. The connection with Coulomb dissociation experiments is discussed and a need for better measurements is pointed out.

PACS: 21.45.+v, 25.10.+s, 25.60.-t, 25.60.Gc

1 Introduction and motivation

During the last years a large effort has been made to investigate the structure of two-neutron halo nuclei whose most prominent examples are the Borromean systems ^6He and ^{11}Li . Their ground-state properties are well reproduced by use of three-body models that describe these nuclei as systems made of an inert core and two-neutrons [1]. These models are also able to reproduce many of the observables measured after fragmentation reactions [2].

Nevertheless several uncertainties concerning especially the structure of ^{11}Li still remain. In a recent work [3] the structure of the two-body unbound system ^{10}Li and its effect on the overall ^{11}Li structure has been investigated. Another question still open refers to the continuum excited spectrum of ^6He and ^{11}Li (these systems do not have bound excited states). For this investigation an appropriate treatment of the three-body wave functions in the continuum and in particular of the resonant states is needed.

Since the interactions involved in ^6He are very well known this nucleus is a perfect test case for the different models describing the properties of two-neutron halo nuclei. The 2^+ resonance with energy and width $(E_R, \Gamma_R) = (0.822 \pm 25, 0.113 \pm 20)$ MeV [4] is well established corresponding to an excitation energy of around 1.8 MeV, as also confirmed in recent ^6He fragmentation reaction experiments [5,6]. Different theoretical calculations reproduce the properties of this 2^+ state [7,8], although they differ in the predicted levels at higher excitation energies.

Coulomb dissociation of ^{11}Li on Pb at 28, 43 and 280 MeV/nucleon shows a prominent peak at about 1 MeV in the differential $B(E1)$ -distribution in several experiments[9–11]. Unfortunately the results of these experiments differ significantly from each other. An excited state at roughly the same excitation energy, $E^* = 1.25 \pm 0.15$ MeV [12], and consistent with the quantum numbers $J^\pi = 0^-$ or 1^- [13] was later found by studying $^{11}\text{Li} + p$ collisions. Together with this level other states appeared at $\sim 3.0, 4.9, 6.4,$ and 11.3 MeV. A more recent experiment [14] investigating the pion capture reaction $^{14}\text{C}(\pi^-, pd)^{11}\text{Li}$ identified excited states for ^{11}Li at excitation energies $1.02 \pm 0.07, 2.07 \pm 0.12,$ and 3.63 ± 0.13 MeV.

On the theoretical side only a rather small number of published calculations of the ^{11}Li spectrum exists. These continuum three-body calculations are technically demanding not least due to the inevitable effects of the hyperfine structure arising from the non-zero spin of the ^9Li core. In addition the neutron-core interaction is uncertain since the spectrum is only incompletely known and the parameters then must be determined indirectly by adjustments to reproduce related observables. A full-scale calculation with realistic parameters was reported in [15]. A number of S -wave poles were found with widths comparable to the real parts of their energies. These poles arise from large distances beyond 130 fm. They are not obtained in any other published computation but on the other hand these large distances were not accurately incorporated in any other numerical investigation. The method in [15] remains on the real radial coordinate axis where the asymptotic boundary condition is enforced by matching the exponentially increasing and oscillating resonance functions at large distance to the proper combination of Hankel functions. This is numerically very difficult and large distance properties must be computed with high accuracy. Alternatives to test or to simplify the computations would be

very valuable.

A paper about the resonances of ^{11}Li appeared recently [16]. The excited states were obtained in a three-body model with separable potential by extension into the continuum. The three lowest excited states of ^{11}Li given in [14] are reproduced without specification of angular momentum and parity as if they were resonance energies measured from threshold. In [17] the effect of the dipole polarizability on the $B(E1)$ strength in ^{11}Li is investigated. The E1 strength was also investigated in [18], and more recently in [19]. The agreement with the experimental $B(E1)$ -strength function is satisfactory, but the excited ^{11}Li spectrum is not computed. These calculations were performed with rather simplified ^{11}Li wave functions where the spin of the core is assumed to be zero. For 1^- excitations this is an important deficiency since the hyperfine splitting can allow low lying dipole excited states with one neutron in each of the lowest neutron-core s and p -states. These three states are very sensitive to the spin splitting of the pairs of $(1^-, 2^-)$ and $(1^+, 2^+)$ -states in ^{10}Li . Models without this feature can then be rather misleading in discussions of both the ^{10}Li and ^{11}Li spectra.

One of the most efficient methods to calculate resonances, introduced in the early 70's, is the complex rotation or complex scaling method [20–22]. The radial coordinates are rotated into the complex plane by an angle θ ($r \rightarrow re^{i\theta}$). When this angle is larger than the argument of a resonance then the divergent wave function corresponding to the resonance becomes convergent, and its rotated wave function shows up after solving the corresponding Schrödinger equation in the same way as a bound state. The details of this method and its application to atomic collisions can be found in [23,24].

Application of the complex rotation method to investigate three-body resonances has already been considered [25,26], and in particular it has been used to investigate different three-body nuclear systems. In [27] the three-body resonances in ^3H and ^3He have been investigated. The same method has also been applied to study the continuum structure of ^9Be and ^9B [28] assuming these nuclei as three-body systems made by two α -particles and a neutron and a proton, respectively. Application to the two-neutron halo nucleus ^6He can be found in [29–31], and in [32] the case of ^{10}He is considered. When available, the agreement with the experimental data is satisfactory. It is remarkable that, even if the method has been applied during the last eight years to different nuclear systems, there are no calculations available concerning the halo nucleus ^{11}Li , whose discovery is widely considered as the starting point of nuclear halo investigations. Only one paper investigating the $3/2^-$ excitations in ^{11}Li with the complex scaling method has very recently been published [33]. In this work the authors point out that the experimental determination of the p -wave resonant state and the s -wave virtual state in ^{10}Li should make the binding mechanism in ^{11}Li clearer. They confirm the previously predicted

roughly equal amount of s and p -wave content within the ^{11}Li [34]. The $3/2^-$ states investigated in [33] correspond to 0^+ excitations, meaning that splitting of the two p -resonances and the two virtual s -states in ^{10}Li play a minor role. As pointed out above, a proper n - ^9Li interaction and an adequate treatment of the spin splitted states in ^{10}Li , are essential ingredients in descriptions of odd parity excitations in ^{11}Li as treated in the present paper.

A suitable method to describe spatially extended and weakly bound three-body systems was introduced in [35,36]. In this method the Faddeev equations are solved in coordinate space by means of the hyperspherical adiabatic expansion. This method is able to reproduce accurately the asymptotics of the wave functions as proved by the fact that it derives the Efimov effect in which an accurate computation of the wave functions at very large distances is essential [35]. A detailed description of the method and applications to atomic and nuclear physics has recently been published [37]. Halo nuclei, as weakly bound and extended systems, are especially appropriate to be described by this method. During the last years we have been investigating both the structure of the ^6He and ^{11}Li ground states and the observables in fragmentation reactions [2,38,39]. The agreement with the experimental data is satisfactory.

Combining the two successful methods of hyperspherical adiabatic expansion and complex scaling is tempting, see [40] for details. The recently established set of model parameters agreeing with known properties of both ^{10}Li and ^{11}Li now allows to fill the gap and compute the continuum spectrum of ^{11}Li with all the decisive features included. The purpose of this paper is to investigate the 1^- excitations in ^{11}Li , i.e. the $1/2^+$, $3/2^+$, and $5/2^+$ continuum states of ^{11}Li obtained by 1^- excitation from to the ground state of $3/2^-$.

We start in section 2 by describing very briefly the main features of the complex scaling method. The specification to the three-body case is shown in section 3, where a brief summary of the hyperspherical adiabatic method is given. The fact that the core of the nucleus (^9Li) is a composite system containing neutrons requires a careful treatment of the Pauli principle. We avoid the neutrons from the halo to occupy Pauli forbidden levels by use of the corresponding phase equivalent potentials, as explained in details in section 3.2. In section 4 we provide the interactions used in the description of ^{11}Li and the structure of the ground state to which they give rise. In section 5 we show the results for the 1^- excitations of ^{11}Li and we finish in section 6 with summary and conclusions.

2 The complex scaling method

For a two-body system the partial wave expansion of the scattering wave function is written as

$$\Psi(\mathbf{p}, \mathbf{r}) = \sqrt{\frac{2}{\pi}} \sum_{\ell} i^{\ell} \frac{u_{\ell}(p, r)}{pr} \sum_m Y_{\ell, m}(\Omega_r) Y_{\ell, m}^*(\Omega_p), \quad (1)$$

where \mathbf{p} and \mathbf{r} are the relative momentum and the relative coordinate, whose directions are defined by the angles Ω_p and Ω_r , respectively. The quantum numbers ℓ and m are the relative angular momentum and its third component. For simplicity we consider particles without spin. The radial wave functions are obtained by solving the Schrödinger equation with the corresponding two-body interaction $V(r)$. For two non-interacting particles the radial wave function $u_{\ell}(p, r)/pr$ is the spherical Bessel function $j_{\ell}(pr)$, and the previous expansion becomes the usual partial wave expansion of a plane wave.

The asymptotic behavior of $u_{\ell}(p, r)$ is given by

$$\frac{u_{\ell}(p, r)}{pr} \longrightarrow \frac{1}{2} \left(h_{\ell}^{(2)}(pr) + S_{\ell}(p) h_{\ell}^{(1)}(pr) \right), \quad (2)$$

where $h_{\ell}^{(1)}(pr) = j_{\ell}(pr) + i\eta_{\ell}(pr)$ and $h_{\ell}^{(2)}(pr) = j_{\ell}(pr) - i\eta_{\ell}(pr)$ are the spherical Hankel functions, and $S_{\ell}(p)$ is the S -matrix. The large distance behavior of $h_{\ell}^{(1)}$ and $h_{\ell}^{(2)}$ is given by $\exp(i(pr - \ell\pi/2))/ipr$ and $\exp(-i(pr - \ell\pi/2))/ipr$, respectively, leading to the following asymptotic behavior for $u_{\ell}(p, r)$:

$$u_{\ell}(p, r) \rightarrow \frac{1}{2i} \left(e^{-i(pr - \ell\pi/2)} + S_{\ell}(p) e^{i(pr - \ell\pi/2)} \right). \quad (3)$$

When the S -matrix is analytically continued into the region of complex values of p the resonances appear as poles of the S -matrix in the lower half-plane of p away from the imaginary axis. Therefore for a resonance the asymptotic behavior of the radial wave function in eq.(2) is given by

$$u_{\ell}(p, r) \longrightarrow \frac{pr}{2} h_{\ell}^{(1)}(pr) \longrightarrow \frac{1}{2i} e^{i(pr - \ell\pi/2)} = \frac{1}{2i} e^{|p|r \sin(\theta_R)} e^{i(|p|r \cos(\theta_R) - \ell\pi/2)}, \quad (4)$$

where $|p|$ and θ_R are the value and the argument of the complex momentum p ($p = |p|e^{-i\theta_R}$).

Since $\sin(\theta_R)$ is positive the corresponding radial wave function of a resonance diverges exponentially. The wave function is therefore non square integrable.

This fact makes it rather difficult to establish numerically the resonant p -value. It is not simple to know precisely the p -value for which the asymptotic behavior of the radial wave function is given only by the exponentially increasing function $h_\ell^{(1)}(pr)$ without any contribution from the exponentially decreasing term $h_\ell^{(2)}(pr)$.

This problem is solved by means of the complex scaling method in which the radial coordinate r is transformed into $re^{i\theta}$. In other words, the radial coordinate in the hamiltonian H is rotated into the complex plane by the angle θ . The asymptotic behavior of the radial solutions of the rotated hamiltonian $H^{(\theta)}$ is now given by the radial rotation of eqs.(2) and (3). In particular for a resonance, according to eq.(4), the asymptotic behavior of the rotated resonant radial wave function $u_\ell^{(\theta)}(p, re^{i\theta})$ is given by

$$u_\ell^{(\theta)}(p, re^{i\theta}) \longrightarrow \frac{1}{2i} e^{-|p|r \sin(\theta - \theta_R)} e^{i(|p|r \cos(\theta - \theta_R) - \ell\pi/2)} \quad (5)$$

Therefore as soon as the scaling angle θ is larger than θ_R the resonant radial wave function decreases exponentially, and it can be computed following the same procedure as for a bound state. Nevertheless the presence of $\sin(\theta - \theta_R)$ in the exponent makes the value r_{max} at which the asymptotics is reached clearly larger than for a “normal” bound state, for which the exponent is simply $-|p|r$.

It is important to realize that one of the main consequences of complex scaling is that while the original hamiltonian H is hermitian the complex rotated hamiltonian $H^{(\theta)}$ is not [24,41]. All the properties and theorems relative to the non-rotated hamiltonian are valid for $H^{(\theta)}$ but using the c -product instead of the ordinary scalar product. The c -product is defined as

$$(f(r)|g(r)) = \langle f^*(r)|g(r) \rangle = \int f(r)g(r)d^3r \quad (6)$$

and, for instance, while the non rotated hamiltonian H satisfies that $\langle f|H|g \rangle = \langle g|H|f \rangle$, the complex scaled hamiltonian $H^{(\theta)}$ satisfies $(f|H^{(\theta)}|g) = (g|H^{(\theta)}|f)$.

In particular, bound states of H appear also as ordinary bound states of the scaled hamiltonian $H^{(\theta)}$ [23]. However, while the radial wave function ψ describing the bound state before rotation is normalized such that $\langle \psi|\psi \rangle = 1$, after rotation the bound state wave function $\psi^{(\theta)}$ is normalized such that

$$(\psi^{(\theta)}(z)|\psi^{(\theta)}(z)) = \int \psi^{(\theta)}(z)\psi^{(\theta)}(z)dz = e^{i\theta} \int_0^\infty \psi^{(\theta)}(re^{i\theta})\psi^{(\theta)}(re^{i\theta})dr = 1 \quad (7)$$

3 The three-body case

To describe a three-body system we start by introducing the usual Jacobi coordinates $(\mathbf{x}_i, \mathbf{y}_i)$

$$\mathbf{x}_i = \sqrt{\frac{1}{m} \frac{m_j m_k}{m_j + m_k}} (\mathbf{r}_i - \mathbf{r}_k), \mathbf{y}_i = \sqrt{\frac{1}{m} \frac{m_i (m_j + m_k)}{m_i + m_j + m_k}} \left(\mathbf{r}_i - \frac{m_j \mathbf{r}_j + m_k \mathbf{r}_k}{m_j + m_k} \right), \quad (8)$$

where $\{i, j, k\}$ is a cyclic permutation of $\{1, 2, 3\}$, m_i , m_j , and m_k are the masses of the three particles in the system, and m is an arbitrary normalization mass that we take to be the nucleon mass.

For each of the three possible sets of Jacobi coordinates the hyperspherical coordinates are defined by the hyperradius $\rho = \sqrt{x_i^2 + y_i^2}$ and the five hyper-angles $\alpha_i = \arctan(x_i/y_i)$ and Ω_{x_i} and Ω_{y_i} that give the directions of \mathbf{x}_i and \mathbf{y}_i .

The three-body wave function is computed by solving the Faddeev equations following the hyperspherical adiabatic expansion described in [37]. The wave function Ψ is expanded in a complete set of generalized angular functions $\Phi_n^{(i)}(\rho, \Omega_i)$

$$\Psi = \frac{1}{\rho^{5/2}} \sum_n f_n(\rho) \sum_{i=1}^3 \Phi_n^{(i)}(\rho, \Omega_i), \quad (9)$$

where the radial expansion coefficients, $f_n(\rho)$, are independent of i and the angular functions are the eigenvectors of the angular part of the Faddeev equations:

$$\hat{\Lambda} \Phi_n^{(i)} + \frac{2m\rho^2}{\hbar^2} V_{jk}(\rho \sin \alpha_i) (\Phi_n^{(i)} + \Phi_n^{(j)} + \Phi_n^{(k)}) = \lambda_n(\rho) \Phi_n^{(i)}, \quad i = 1, 2, 3 \quad (10)$$

where the angular operator $\hat{\Lambda}$ can be found for instance in [37] and V_{jk} is the interaction between particles j and k .

The radial coefficients $f_n(\rho)$ are obtained from a coupled set of differential equations in which the angular eigenvalues $\lambda_n(\rho)$ enter as effective potentials:

$$\left[\frac{d^2}{d\rho^2} - \frac{2mE}{\hbar^2} + \frac{1}{\rho^2} \left(\lambda_n(\rho) + \frac{15}{4} \right) \right] f_n(\rho) + \sum_{n'} \left(-2P_{nn'}(\rho) \frac{d}{d\rho} - Q_{nn'}(\rho) \right) f_{n'}(\rho) = 0, \quad (11)$$

where the functions P and Q also can be found in [37].

3.1 Complex coordinate rotation

For a system of three particles in the continuum the S -matrix has known analytical properties similar to a two-particle multichannel problem. The radial wave functions must then be labeled with two indexes, one of them (n) being the usual index on the components, and a second index n' labeling all the possible asymptotic behaviors and therefore labeling different total wave functions in eq.(9). We can actually interpret n and n' as labels for the ingoing and outgoing three-body channels.

The asymptotic behavior of the radial three-body continuum wave functions is given by:

$$f_{nn'}(\rho) \longrightarrow \sqrt{\frac{m\rho}{4\hbar^2}} \left(\delta_{nn'} H_{K+2}^{(2)}(\kappa\rho) + S_{nn'} H_{K+2}^{(1)}(\kappa\rho) \right), \quad (12)$$

where $\kappa = \sqrt{2mE/\hbar^2}$, E is the three-body energy and $H_{\mu}^{(1,2)}(\kappa\rho)$ are the Hankel functions. The value of the hypermomentum K is defined by the asymptotic value of the eigenfunction $\lambda_n(\rho)$ associated to channel n , that is given by $K(K+4)$.

Again, when the S -matrix is analytically continued into the complex κ -plane resonances show up as poles of the S -matrix in the lower half-plane and away from the imaginary axis. Therefore the asymptotics of the radial resonance wave function is given only by the Hankel function $H_{K+2}^{(1)}(\kappa\rho)$ that goes at large distances as $\sqrt{2/\pi\kappa\rho} \exp(i(\kappa\rho - K\pi/2 + 3\pi/4))$. Writing now the complex wave number κ as $|\kappa|e^{-i\theta_R}$ we find for the asymptotics of $f_{nn'}(\rho)$ the expression

$$f_{nn'}(\rho) \longrightarrow e^{|\kappa|\rho \sin(\theta_R)} e^{i(|\kappa|\rho \cos(\theta_R) - K\pi/2 + 3\pi/4)}, \quad (13)$$

that is equivalent to eq.(4).

Again the exponential divergence in the resonance radial wave function can be eliminated by use of the complex scaling method. Rotation of the Jacobi coordinates by an angle θ amounts to rotation of the hyperradius ρ into $\rho e^{i\theta}$, since all the five hyperangles remain unchanged. Therefore, as in the two-body case, the rotated radial wave function of the three-body resonance has the asymptotic behavior given by

$$f_{nn'}(\rho e^{i\theta}) \rightarrow e^{-|\kappa|\rho \sin(\theta - \theta_R)} e^{i(|\kappa|\rho \cos(\theta - \theta_R) - K\pi/2 + 3\pi/4)}, \quad (14)$$

that decreases exponentially for values of θ larger than θ_R . As a consequence,

combining the complex scaling with the hyperspherical adiabatic expansion method described in [37] will permit calculation of the complex energy of a three-body resonance ($E = E_R - i\Gamma_R/2$, where E_R is the resonance energy and Γ_R is the width), as well as its rotated wave function.

After complex scaling the effective potentials $\lambda_n(\rho)$ entering in the radial part of the Faddeev equations (eq.(11)) become complex quantities, and depend as well on the complex rotation angle θ . As shown in [37] at short distances the non-rotated λ 's behave as

$$\lambda(\rho) \xrightarrow{\rho \rightarrow 0} K(K+4) - b\rho^2, \quad (15)$$

where K is the hypermomentum and b is a positive constant for attractive potentials. After transformation of ρ into $\rho e^{i\theta}$ we see that the real part of the rotated λ 's goes as

$$\text{Re}(\lambda(\rho e^{i\theta})) \xrightarrow{\rho \rightarrow 0} K(K+4) - b\rho^2 \cos(2\theta) \quad (16)$$

and therefore at $\rho = 0$ the real part of the rotated λ -spectrum corresponds to the hyperspherical spectrum $K(K+4)$, where for 1^- excitations K has to be odd. In the same way the imaginary part of the rotated λ 's goes like

$$\text{Im}(\lambda(\rho e^{i\theta})) \xrightarrow{\rho \rightarrow 0} -b\rho^2 \sin(2\theta) \quad (17)$$

and therefore all of them start at zero and take negative values at short distances. We also see that the larger the rotation angle θ the higher the slope of the imaginary part of the λ function at short distances.

At large distances, assuming that we are dealing with Borromean systems, the λ functions behave as [37]

$$\lambda(\rho) \xrightarrow{\rho \rightarrow \infty} K(K+4) - \frac{c}{\rho^{1+2\ell_0}}, \quad (18)$$

where c is a positive constant for attractive potentials and ℓ_0 is an integer. We then see that after complex scaling the real part of the rotated λ 's is again recovering the hyperspherical spectrum at infinity, while the imaginary part goes like

$$\text{Im}(\lambda(\rho e^{i\theta})) \xrightarrow{\rho \rightarrow \infty} c \sin((1+2\ell_0)\theta) / \rho^{1+2\ell_0}. \quad (19)$$

Therefore the imaginary part of the complex rotated λ 's goes to zero at infinity from above. Since at short distances the imaginary part is negative we conclude

that for all the rotated λ 's in the expansion (11) the imaginary part has an oscillatory behavior, starting at zero, becoming negative, crossing afterwards the zero axis, and going finally again to zero at infinity from above.

3.2 The Pauli principle and complex scaled phase equivalent potentials

An accurate treatment of the Pauli principle is one of the most important points when describing few-cluster systems where the clusters are composite structures containing identical fermions. In [42] we have shown that the use of phase equivalent potentials [43–46] is an appropriate method to implement the Pauli principle in three-body calculations based on the adiabatic hyperspherical approach.

Phase equivalent potentials are constructed as follows. Let us consider two particles interacting with each other via a potential $V(r)$ such that the two-body system has one or several bound states, where the radial wave function of its lowest bound state is $\psi_{\ell s j}(r)$. It is then possible to construct a second potential with exactly the same phase shifts as $V(r)$ for any value of the two-body energy and such that the new potential has the same bound state spectrum except the one described by $\psi_{\ell s j}(r)$, that is removed. This new phase equivalent potential has the form [46]:

$$V^{(pe)}(r) = V(r) - \frac{(\hbar c)^2}{\mu} \frac{d^2}{dr^2} \ln \left(\int_0^r |\psi_{\ell s j}(r')|^2 dr' \right), \quad (20)$$

where μ is the reduced mass of the two particles.

Simultaneous application of the procedure described in [42] to treat the Pauli principle and the complex scaling method obviously requires the complex scaling of the corresponding phase equivalent potentials. After complex scaling the bound states of the original potential are also present, and in particular those bound states forbidden by the Pauli principle should be removed from the calculation. To do this we construct the corresponding phase equivalent potential where the forbidden state has been removed according to eq.(20), but where the radial coordinate r is replaced by the scaled coordinate $z = re^{i\theta}$. Therefore the complex rotated phase equivalent potential is given by:

$$V^{(pe)}(z) = V(z) - \frac{(\hbar c)^2}{\mu} \frac{d^2}{dz^2} \ln \left(\int_{z'=0}^{z'=z} (\psi_{\ell s j}^{(\theta)}(z'))^2 dz' \right) =$$

^{10}Li spectrum

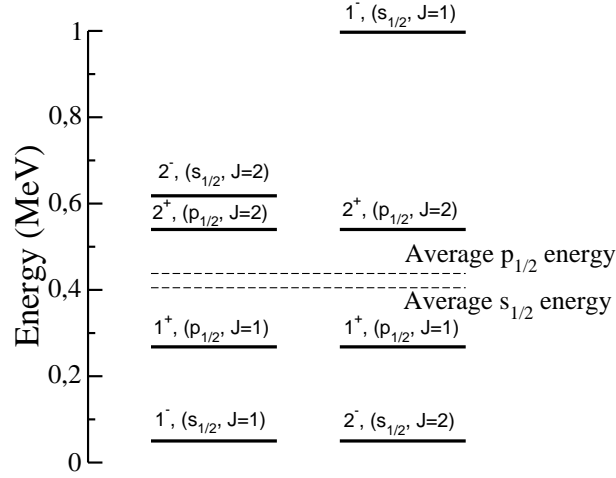


Fig. 1. ^{10}Li spectra obtained with the neutron- ^9Li interaction used in the three-body calculation.

$$V(z) - \frac{(\hbar c)^2}{\mu} e^{-i\theta} \frac{d^2}{dr^2} \ln \left(\int_{r'=0}^{r'=r} (\psi_{\ell s j}^{(\theta)}(r' e^{i\theta}))^2 dr' \right) \quad (21)$$

where $\psi_{\ell s j}^{(\theta)}(r e^{i\theta})$ is the complex rotated radial wave function of the Pauli forbidden bound state, that is normalized according to eq.(7). After performing the second derivative one gets the following final expression for the complex scaled phase equivalent potential:

$$V^{(pe)}(r e^{i\theta}) = V(r e^{i\theta}) - \frac{(\hbar c)^2}{\mu} e^{-i\theta} \left[\frac{2\psi_{\ell s j}^{(\theta)}(r e^{i\theta}) \frac{d\psi_{\ell s j}^{(\theta)}(r e^{i\theta})}{dr}}{\int_0^r (\psi_{\ell s j}^{(\theta)}(r' e^{i\theta}))^2 dr'} - \frac{(\psi_{\ell s j}^{(\theta)}(r e^{i\theta}))^4}{\left(\int_0^r (\psi_{\ell s j}^{(\theta)}(r' e^{i\theta}))^2 dr' \right)^2} \right]. \quad (22)$$

4 Bound ^{11}Li structure

In ref.[3] we have investigated the structure of the unbound nucleus ^{10}Li and its connection with the ground state properties of ^{11}Li . We have used a neutron- ^9Li potential consistent with the structure of the ^9Li core and the energies and quantum numbers of the experimentally established two-body resonances and virtual states in ^{10}Li . In particular the neutron-core interaction is reproducing a 2^+ state at 0.54 MeV and a virtual state (either 1^- or 2^- state) at 50 keV¹. In this work we have then investigated the range of energies of the

¹ Energies of virtual s-states are strictly negative. However, to avoid confusion with bound states we use the absolute values. Therefore in the spectrum the virtual states then appear among resonances although they do not show up in the cross section with the characteristic resonance bump.

1^+ p -resonance and the second virtual state still consistent with the known properties of ^{11}Li , i.e. the existence of one and only one bound state with $J^\pi = \frac{3}{2}^-$, a binding energy of ~ 0.300 keV, and a p -wave content of $\sim 40\%$. In this way we have determined a set of possible neutron- ^9Li interactions for which we have computed the ^{10}Li invariant mass spectrum after fragmentation of ^{11}Li on a carbon target. This observable is especially interesting because it is probably the most sensitive one to the energy levels of each of the two-body subsystems contained in the three-body nucleus. Comparison of the computed and experimental invariant mass spectra was then used to establish the most likely spectra for ^{10}Li . In ref.[3] we have then concluded that together with the 2^+ p -resonance at 0.54 MeV ^{10}Li must have a second p -resonance (1^+) at an energy of 0.35 ± 0.15 MeV. For the virtual states one of the two possible levels (1^- or 2^-) is placed at a low energy (~ 50 keV), while the second one must be at an energy of 0.80 ± 0.30 MeV.

To be precise in the present work we have used the potential parameters corresponding to the spectra c and d in the upper part of fig.6 in [3]. These two spectra are shown in fig.1, and they are such that both of them have a 2^+ -resonance at 0.54 MeV and a 1^+ -resonance at 0.25 MeV, consistent with the 1^+ level at 0.24 ± 0.06 MeV observed in [47]. The difference between both spectra is that in one of them the virtual s -state at 50 keV is the 1^- -state (left part of fig.1), while for the other one it is the 2^- -state. Both spectra are consistent with all experimental information and only small modifications are allowed to maintain this agreement.

These two spectra are obtained with a neutron- ^9Li interaction of the form

$$V_{nc}^{(\ell)}(r) = V_c^{(\ell)}(r) + V_{ss}^{(\ell)}(r)\langle \mathbf{s}_n \cdot \mathbf{s}_c \rangle + V_{so}^{(\ell)}(r)\boldsymbol{\ell}_{nc} \cdot \mathbf{s}_n, \quad (23)$$

where $\langle \mathbf{s}_n \cdot \mathbf{s}_c \rangle = \langle \ell_{nc}, j_n, J | \mathbf{s}_n \cdot \mathbf{s}_c | \ell_{nc}, j_n, J \rangle$, \mathbf{s}_n and \mathbf{s}_c are the intrinsic spins of the neutron and the core, $\boldsymbol{\ell}_{nc}$ is their relative orbital angular momentum, j_n is the coupled momentum of ℓ_{nc} and s_n , and J is the total angular momentum obtained after coupling of j_n and the spin of the core s_c .

In the calculation s -waves and p -waves have been included. The radial central, spin-spin, and spin-orbit potentials are taken to be gaussians with range equal to 2 fm. The strengths of the gaussians are -94.0 MeV and -79.64 MeV for the central s and p -potentials respectively. For the spin-orbit and spin-spin p -potentials the strength of the gaussians is -13.12 MeV and 1.10 MeV, respectively. For the spin-spin potential for s -waves we take 6.85 MeV and -11.4 MeV when the 1^- and 2^- virtual states respectively are placed at 50 keV. The neutron-neutron interaction is given in [48].

The potentials specified above are such that the $s_{1/2}$ -interaction has a low-lying virtual state at 50 keV and a deeply bound state while the $p_{3/2}$ -interaction

Table 1

Components used in the calculation of the $J^\pi = \frac{1}{2}^+$ state. K_{max} is the maximum value of the hypermomentum K used in the hyperspherical expansion. The left part of the table refers to the components in the Jacobi set where \mathbf{x} connects the two halo neutrons, while in the right part \mathbf{x} connects the ${}^9\text{Li}$ core and one neutron.

ℓ_x	0	1	1	0	0	0	1	1	1
ℓ_y	1	0	0	1	1	1	0	0	0
L	1	1	1	1	1	1	1	1	1
s_x	0	1	1	1	1	2	1	1	2
S	3/2	1/2	3/2	1/2	3/2	3/2	1/2	3/2	3/2
K_{max}	181	121	121	121	181	121	121	121	181

Table 2

As in table 1 for the $J^\pi = \frac{3}{2}^+$ state.

ℓ_x	0	1	1	1	0	0	0	0	1	1	1	1
ℓ_y	1	0	0	0	1	1	1	1	0	0	0	0
L	1	1	1	1	1	1	1	1	1	1	1	1
s_x	0	1	1	1	1	1	2	2	1	1	2	2
S	3/2	1/2	3/2	5/2	1/2	3/2	3/2	5/2	1/2	3/2	3/2	5/2
K_{max}	201	121	121	121	181	181	181	181	121	121	121	121

has a bound state at -4.1 MeV, that is the neutron separation energy in ${}^9\text{Li}$ [49]. Since the $s_{1/2}$ -shell and the neutron $p_{3/2}$ -shell are completely filled by the neutrons in the ${}^9\text{Li}$ nucleus these states are forbidden by the Pauli principle when adding more neutrons as for ${}^{10}\text{Li}$ and ${}^{11}\text{Li}$. As mentioned in the previous section the Pauli principle is taken into account by substituting the $s_{1/2}$ and the $p_{3/2}$ interactions by the corresponding phase equivalent potentials.

Another feature to be considered is that the two-body interactions alone underbind the three-body nucleus ${}^{11}\text{Li}$. This is a well known general problem for few-body systems [50]. To recover the experimental value of the binding energy we introduce a phenomenological three-body interaction that accounts for the polarization of the particles. The shape of this three-body force is a gaussian in hyperradius with a range equal to 3 fm and a strength -3.9 MeV.

5 Dipole excited states

To compute the 1^- excited states in ${}^{11}\text{Li}$ we follow exactly the same procedure as for the ${}^{11}\text{Li}$ ground state but with the complex scaling transformation

Table 3

As in table 1 for the $J^\pi = \frac{5}{2}^+$ state.

ℓ_x	0	1	1	0	0	0	1	1	1
ℓ_y	1	0	0	1	1	1	0	0	0
L	1	1	1	1	1	1	1	1	1
s_x	0	1	1	1	2	2	1	2	2
S	3/2	3/2	5/2	3/2	3/2	5/2	3/2	3/2	5/2
K_{max}	181	121	121	181	181	181	121	121	121

described in section 3. We use then the hyperspherical adiabatic expansion method to solve the complex scaled Faddeev equations in coordinate space. The Faddeev equations are solved with the complex scaled neutron–neutron and neutron–core interactions described in the previous section. The Pauli principle is taken into account as described in section 3.2 by use of the corresponding complex scaled phase equivalent potentials.

The ^{11}Li ground state has the quantum numbers $J^\pi = \frac{3}{2}^-$, and therefore a 1^- excitation will lead to states with spin and parity $\frac{1}{2}^+$, $\frac{3}{2}^+$, or $\frac{5}{2}^+$. The only difference between the calculations of these three states is in the components included, since for each of them the quantum numbers of each component have to be consistent with the total spin and parity. In tables 1, 2, and 3 we specify the components used for the $\frac{1}{2}^+$, $\frac{3}{2}^+$, and the $\frac{5}{2}^+$ states, respectively. In each table the left part shows the components used in the Jacobi set where the \boldsymbol{x} -coordinate connects the neutrons, while in the right part the components refer to the two Jacobi sets in which \boldsymbol{x} connects one of the neutrons and the core.

5.1 Complex rotated hyperspherical adiabatic potentials

The general behavior at short and large distances of the λ -effective potentials entering in the radial equations (11) is given by eqs.(15) to (19). This general behavior can be observed in the complex scaled λ 's obtained for the $1/2^+$, $3/2^+$, and $5/2^+$ states in ^{11}Li . In all the calculations shown in this work we have considered two λ 's in the expansion (11), although inclusion of the second λ is not changing the results significantly. Typically the second λ is giving from 5 to 10% of the rotated wave function. In fig.2 we show the real and imaginary parts of the most contributing $\lambda(\rho)$ for three different values of the rotation angle $\theta = 0.25$, $\theta = 0.30$, and $\theta = 0.35$. The left, central, and right parts of the figure correspond to the $1/2^+$ state, the $3/2^+$ state, and the $5/2^+$ state, respectively. The potentials used in the calculations produce the ^{10}Li spectrum described in section 4, i.e., a 1^+ p -resonance at 0.25 MeV, a 2^+ p -resonance at

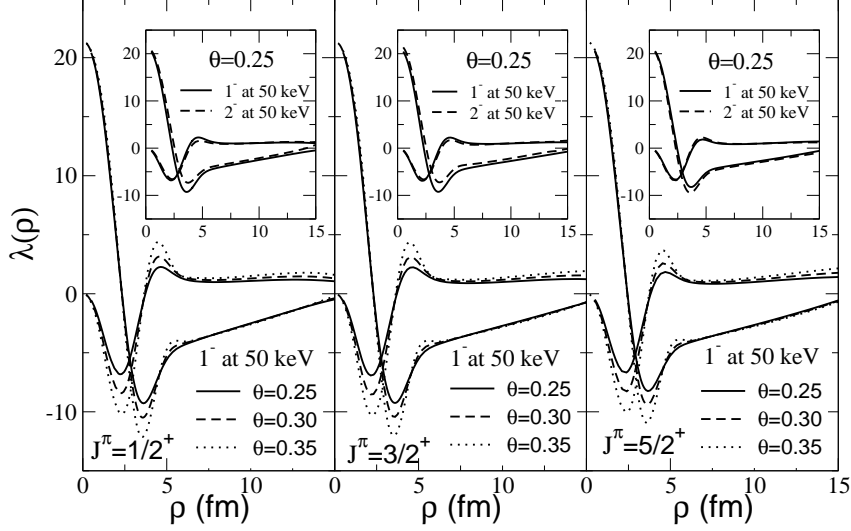


Fig. 2. Deepest rotated λ -function for the $1/2^+$ state (left) the $3/2^+$ state (middle), and $5/2^+$ state (right) in ^{11}Li . In the external plots we show the complex λ 's for rotation angles $\theta = 0.25$ (solid), $\theta = 0.30$ (dashed), and $\theta = 0.35$ (dotted) for the ^{10}Li spectrum in the left part of fig.1. The real parts are the curves starting at 21, while the imaginary parts start at zero. In the insets we compare for $\theta = 0.25$ the deepest λ for the left (solid) and right (dashed) ^{10}Li spectra in fig.1.

0.54 MeV, and a low-lying virtual s -state at 50 keV. The λ -functions shown in the external parts of the figures correspond to the 1^- level in ^{10}Li at 50 keV (^{10}Li spectrum in the left part of fig.1). In the inner part of the figures we compare for $\theta = 0.25$ the lowest λ functions when the 1^- (solid line) and the 2^- (dashed line) is at 50 keV.

According to eqs.(16) and (18) the real part of the rotated λ 's have to coincide with the hyperspherical spectrum $K(K+4)$ at both $\rho = 0$ and $\rho = \infty$. Since we are considering negative parity states only odd values of K are then possible. In the figure the real part of the λ 's is given by the curves starting in all the three cases at 21. This value corresponds to the hyperspherical level with $K = 3$. At large distances the real part of the λ -function goes to 5, that is the level corresponding to $K = 1$ (not reached in the figure where the maximum value of ρ is only 15 fm). The real part of the lowest rotated λ does not start at 5 ($K = 1$) for $\rho = 0$, since this λ is Pauli forbidden and excluded by our use of the phase equivalent potentials. If this Pauli forbidden state had not been suppressed the lowest λ would start at 5, and parabolically diverge to $-\infty$ at large distances [42]. In the figure we also show the imaginary part of the lowest λ 's. They behave at short and large distances as dictated by eqs.(17) and (19). They start at zero, become negative according to $-\rho^2 \sin(2\theta)$, they cross the zero axis, and at large distances they return to zero from the positive side.

In the inner part of the figures we compare for $\theta = 0.25$ the deepest λ when

the 1^- (solid lines) and 2^- (dashed lines) s -states are at 50 keV. We observe in the figure insets that for the $1/2^+$ and the $3/2^+$ excited states the presence of a low-lying 1^- s -state is making the lowest λ slightly deeper than when we have the 2^- level at 50 keV. For the $5/2^+$ state it is the opposite, the 2^- level in ^{10}Li favors a deeper λ -function. The reason is that $1/2^+$, but not $5/2^+$, can be constructed when both neutron-core states simultaneously are relative 1^- -states and vice versa, $5/2^+$, but not $1/2^+$, can be constructed when both neutron-core states simultaneously are relative 2^- -states. For $3/2^+$ both neutrons can simultaneously be coupled to the core in each of the 1^- or 2^- states, but the overlap is larger for the 1^- than for the 2^- -state.

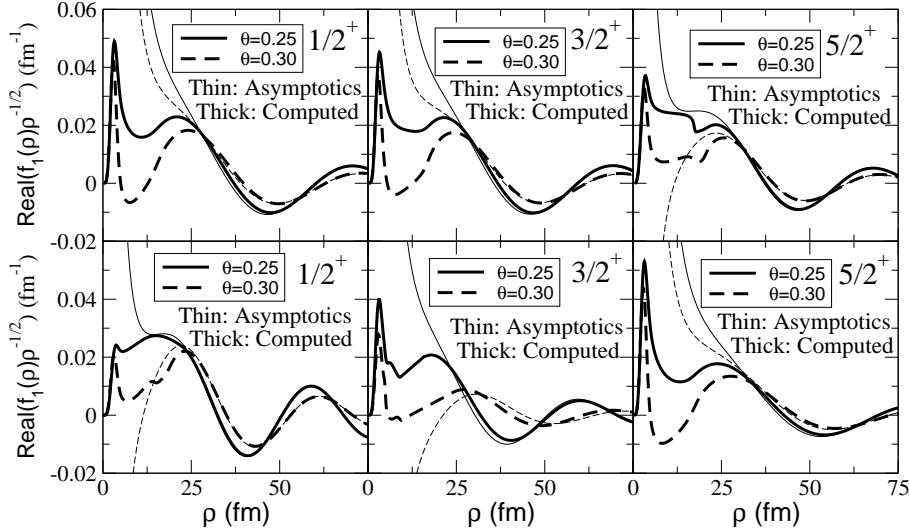


Fig. 3. Real part of the rotated radial wave function associated with the rotated lowest λ -function (see eq.(11)). Solid and dashed lines correspond to a rotation angle of $\theta = 0.25$, and $\theta = 0.30$, respectively. Thick lines are the computed wave functions, and the thin lines are the asymptotic functions $H_{K+2}^{(1)}(\kappa\rho)$, see eq.(12). The left, middle, and right parts of the figure show the wave functions corresponding to the 1^- excited states in ^{11}Li with $J^\pi = 1/2^+$, $3/2^+$ and $5/2^+$, respectively. The upper part of the figure correspond to a 1^- virtual s -state in ^{10}Li at 50 keV, while in the lower part a 2^- virtual s -state at 50 keV in ^{10}Li is assumed. In all the cases a 2^+ p -resonance in ^{10}Li at 0.54 MeV and a 1^+ p -resonance in ^{10}Li at 0.25 MeV are assumed.

5.2 Complex rotated radial wave functions

The effective radial potential arising from the λ -functions in fig.2 are used in eq.(11). In figs.3 and 4 we show the real and imaginary parts of the complex rotated radial wave function $f_1(\rho)$ associated with the deepest λ -function. The wave function has been divided by $\sqrt{\rho}$. We also show the asymptotic wave functions, which according to eq.(12) for a resonance after complex rotation is given by $H_{K+2}^{(1)}(|\kappa|\rho e^{i(\theta-\theta_R)})$.

The asymptotics is reached at values of the hyperradius smaller than 50 fm, except for the $J^\pi = 3/2^+$ -state where a 2^- s -state is at 50 keV in ^{10}Li (middle-low part of the figure). In this case the asymptotics is reached at $\rho \approx 80$ fm. From eq.(14) we know that the exponential decrease of the rotated radial wave functions at large distances is governed by the exponent $-|\kappa|\rho \sin(\theta - \theta_R)$. Therefore larger values of the rotation angle θ will produce a faster decrease of the radial wave functions as seen in both figs.3 and 4.

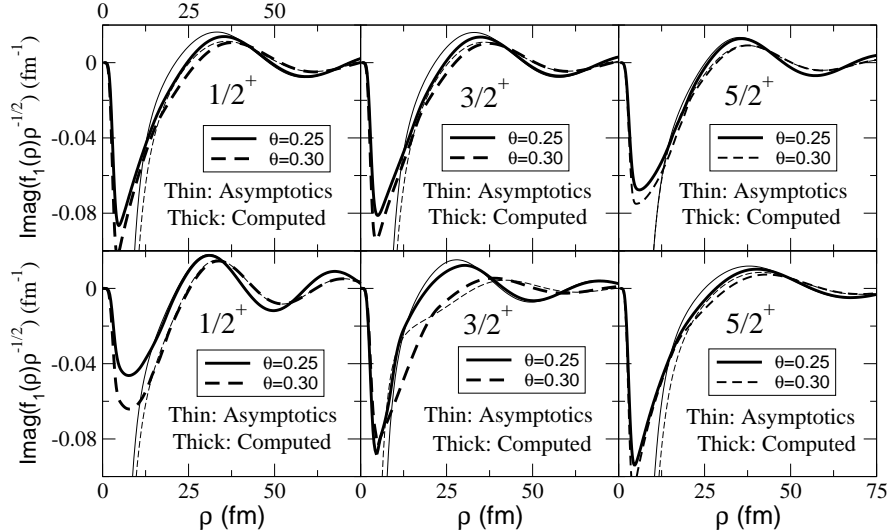


Fig. 4. The same as fig.3 but for the imaginary part of the rotated radial wave functions.

The complex scaled radial wave functions exhibit peaks at short distances. In fact this is a manifestation of the three-body resonance. Due to the faster decrease of the wave functions for large values of θ this peak is more pronounced for $\theta = 0.30$ than for $\theta = 0.25$. The peak at short distances is especially narrow and the three-body resonance is well-defined for the real part of the radial wave functions in fig.3. The peak structure at short distances is also pronounced but much broader for the imaginary part of the wave functions shown in fig.4. In some cases the radial wave functions present strange kinks, as in the upper part of fig.3 for $J^\pi = 5/2^+$ and $\theta = 0.25$ at $\rho \approx 15$ fm. This is produced by a sharp crossing in the two effective potentials (the λ -functions) included in eq.(11). Nevertheless this crossing does not influence the resonance energy as demonstrated by independence of θ for values where the crossing is smoother.

5.3 Dipole excitations

In table 4 we show the resonance energies (E_R) and widths (Γ_R) of the 1^- excitations in ^{11}Li obtained after solving the Faddeev equations by use of the complex rotated hyperspherical adiabatic method. The left part of the table

Table 4

Computed energies (E_R) and widths (Γ_R) for the lowest excited 1^- states in ^{11}Li for $J^\pi = 1/2^+$, $J^\pi = 3/2^+$, and $J^\pi = 5/2^+$. Columns 2 and 3 are obtained assuming a 1^- virtual s -state in ^{10}Li at 50 keV, while in columns 4 and 5 it is a 2^- s -state the one at 50 keV. The energy of the 1^+ p -resonance in ^{10}Li is 0.25 MeV in columns 2 and 4, and 0.45 MeV in columns 3 and 5.

	(E_R, Γ_R) (MeV)			
	1^- at 50 keV		2^- at 50 keV	
$E(1^+)$	0.25 MeV	0.45 MeV	0.25 MeV	0.45 MeV
$\frac{1}{2}^+$	(0.41, 0.26)	(0.44, 0.29)	(0.65, 0.59)	(0.70, 0.65)
$\frac{3}{2}^+$	(0.44, 0.27)	(0.52, 0.39)	(0.58, 0.35)	(0.62, 0.55)
$\frac{5}{2}^+$	(0.51, 0.31)	(0.63, 0.46)	(0.32, 0.15)	(0.42, 0.25)

(columns 2 and 3) corresponds to a neutron- ^9Li interaction producing a 1^- virtual s -state in ^{10}Li at 50 keV, while in the right part (columns 4 and 5) a 2^- state is at 50 keV. The excitation energy (E^*) is obtained after summation of the two-neutron separation energy in ^{11}Li to the resonance energy ($E^* = E_R + 0.3$ MeV). These numbers have been obtained after scanning the complex plane for values of the complex energy up to 1.5 MeV, and using a maximum value of the complex rotation angle θ of 0.35 rads. We have then to be aware that resonances corresponding to higher energies or with argument larger than 0.70 rads could have been missed in the calculation.

We start by assuming the ^{10}Li structure shown in fig.1, i.e. a 1^+ p -resonance at 0.25 MeV and a 2^+ p -resonance at 0.54 MeV. These numbers are consistent with the experimental data given in [47]. In columns 2 and 4 of table 4 we give the computed ^{11}Li resonance energies and widths for the ^{10}Li spectra in the left and right parts of fig.1, respectively. From the resonance energies shown in table 4 we see that only the $1/2^+$ excited state in column 4, and to a lower extent the $3/2^+$ state in the same column, gives rise to an excitation energy of around 1 MeV in agreement with the available experimental values ($E^* = 1.25 \pm 0.15$ [12] and $E^* = 1.02 \pm 0.07$ [14]). The three excited states given in column 2 have an excitation energy a bit lower, between 0.7 and 0.8 MeV. Finally, the $5/2^+$ state in column 4 has an excitation energy of around 0.6 MeV, clearly below the experimental value.

The computed resonances in table 4 are similar to the lowest ones obtained in [15] by a different method but with realistic interactions and in particular with the important hyperfine splitting. In [15] several resonances of the same spin and parity were found in contrast to all other computations including the present one. Large distances are responsible for these additional resonances. Accurate treatment of distances well beyond 100 fm is required and no other computation has achieved that. Unfortunately the complex coordinate rota-

tion increases the range of the rotated interaction and thereby increase the difficulties of treating large distances. The advantage is that the boundary condition for the resonance wave functions are transformed into the exponentially vanishing bound state condition.

Switching off the spin splitting interaction, it is still possible to maintain essentially all three-body related ^{11}Li ground state structure and reaction properties [3]. Then the two-body resonances of ^{10}Li all must be at the average positions indicated in fig.1 around 0.4 MeV. The three 1^- -resonances then reduce to only one, that after the corresponding calculation without the spin splitting neutron–core interaction is found to be at $(E_R, \Gamma_R) = (0.48, 0.33)$ MeV. This energy corresponds approximately to the statistically averaged values of the $1/2^+$, $3/2^+$ and $5/2^+$ resonance energies given in columns 2 and 4 of table 4. In these averages the weights of the $1/2^+$, $3/2^+$, and $5/2^+$ energies are $1/6$, $2/6$, and $3/6$, respectively, according to the different number of spin projections in each case. The average values are then $(0.47, 0.29)$ MeV and $(0.46, 0.29)$ MeV for the second and fourth columns in table 4, respectively.

However, the properties of ^{10}Li are inconsistent with the parameter choice of zero spin splitting and two low-lying resonances of opposite parity in the ^{10}Li spectrum. For the ground state of ^{11}Li only the average positions are important since the two neutrons essentially are forced to couple to 0^+ and therefore simultaneously occupy both low and high lying two-body resonance states. For the 1^- -excitations essentially only one level in each pair of these spin split states need to be occupied to produce the excited states. Therefore the finite core spin and the subsequent spin splitting is crucial for breaking the degeneracy of the 1^- -states. In some cases some of the splitted levels might be lowered substantially compared to results of zero core-spin computations with the same average two-body resonance positions.

It is important to emphasize that in [3] we concluded that the most likely spectrum for ^{10}Li has a 1^+ p -resonance with energy of 0.35 ± 0.15 MeV. Therefore a 1^+ p -resonance at 0.25 MeV as chosen in the present calculations is a lower limit of the predicted energy range. The effect of a higher energy for the 1^+ resonance in ^{10}Li can be seen in the columns 3 and 5 of table 4, where we have chosen an energy of 0.45 MeV for the 1^+ p -resonance. Of course this higher energy value is producing higher energies for the three–body excited states. In some cases, as for the $5/2^+$ -states, the energy increase can reach even more than 100 keV. In this case the lowest excitation energy is 0.72 MeV. Again, a calculation of the resonance energy suppressing the spin–splitting interaction is reducing the resonances in columns 3 and 5 in table 4 to a single resonance with energy and width of $(0.56, 0.43)$ MeV that is similar to the statistically averaged energies of $(0.56, 0.41)$ and $(0.53, 0.42)$ MeV obtained with the resonance values in columns 3 and 5, respectively. Therefore, by simple comparison of the computed three–body excitation energies for ^{11}Li and the experimental

value of 1 MeV, it seems that the 1^+ p -resonance energy in ^{10}Li is more likely at an energy higher than the 0.25 MeV measured in [47].

The structure of the degenerate 1^- -resonance for zero spin-splitting corresponds to an equal probability for neutron-core s and p -waves. This is simply because essentially only s and p -waves contribute and a three-body 1^- -excitation has to be made of neutron-core $l_x = 0, 1$ and the corresponding $l_y = 1, 0$. The antisymmetry of the two neutrons then requires roughly 50% of both the s and p -wave neutron-core relative states. This equal division is therefore independent of the average positions of the neutron-core p -resonance and virtual s -state. The finite core-spin distributes the probabilities on more components depending on the coupling necessary to produce the total angular momentum of the three-body resonance, see tables 1, 2 and 3.

The results shown in table 4 are independent of the rotation angle used in the calculation. In particular, the numbers given in the table have been obtained with rotation angles $\theta = 0.25$, $\theta = 0.30$, and $\theta = 0.35$. Another point is the possible three-body effects that are not taken into account in the calculation. It is well known that computation of three-body ground states by use of pure two-body interactions generally underbinds the three-body system. This problem is solved by inclusion of an attractive three-body potential in the radial equation (11) that accounts for the polarization of the particles that are beyond that described by the effective two-body interactions. The results shown in table 4 have been obtained without use of a three-body potential.

Including a three-body potential of range 3 fm essentially leaves the resonance parameters unchanged. The reason is that the generalized centrifugal barrier already provide a rather repulsive potential at distances smaller than 3 fm. The three-body potential is then only marginally changing the effective radial potential and has with this range and a reasonable strength very little influence. This may reflect that a three-body potential, at least for non-zero orbital angular momentum states, should depend on other space variables than the hyperradius, i.e. directions and relative size of the \mathbf{x} and \mathbf{y} coordinates. Effectively this probably corresponds to a larger range due to the resulting different asymmetric geometry related to non-zero angular momentum. This also may result in a potential with both attractive and repulsive regions. Although the effect still has to be small the resonance positions could then either move up or down.

5.4 Coulomb dissociation cross section

The cross section for Coulomb excitation of electric dipole states in the projectile nucleus is given by [51]

$$\frac{d\sigma_c}{dE^*} = \frac{N_{E1}(E^*)}{E^*} \sigma_{E1}(E^*) = \frac{N_{E1}(E^*)}{\hbar c} \frac{16\pi^3}{9} \frac{dB(E1)}{dE^*}, \quad (24)$$

where $\sigma_{E1}(E^*)$ is the photonuclear cross section, $B(E1)$ is the dipole strength function, and the number of equivalent photons $N_{E1}(E^*)$ is given by

$$N_{E1}(E^*) = \frac{2}{\pi} Z_1^2 \alpha \left(\frac{c}{v}\right)^2 \left[\xi K_0(\xi) K_1(\xi) - \frac{v^2 \xi^2}{2c^2} (K_1(\xi)^2 - K_0(\xi)^2) \right], \quad (25)$$

where K_0 and K_1 are the modified Bessel functions, Z_1 is the charge of the projectile, α is the fine structure constant, and

$$\xi = \frac{E^* R}{\hbar \gamma v}; \quad R = R_1 + R_2 + \frac{\pi a}{2}; \quad a = \frac{Z_1 Z_2 \alpha}{2E_{kin}}, \quad (26)$$

v is the velocity of the projectile, $\gamma = (1 - v^2/c^2)^{-1/2}$, R_1 and R_2 are the radii of projectile and target, respectively, Z_2 is the charge of the target, and a is half the distance of closest approach between projectile and target. E_{kin} is the kinetic energy of the projectile.

The connection between the measured cross section $d\sigma_M/dE$ and the true cross section $d\sigma_c/dE$ is given by

$$\frac{d\sigma_M}{dE}(E) = \int \frac{d\sigma_c}{dE'}(E') \varepsilon(E', E) dE', \quad (27)$$

where $\varepsilon(E', E)$ represents the response of the detector system. The decay energy E is related to the excitation energy E^* according to $E^* = E + S_{2n}$, where S_{2n} is the two-neutron separation energy.

Assuming that the Coulomb dissociation process takes place through a three-body resonance decay mechanism in which only the resonances are populated in the final state, the photonuclear cross section σ_{E1} can be parameterized with a Breit–Wigner function given by

$$\sigma_{E1}(E) = \frac{\sigma_m \Gamma(E)}{(E - E_R)^2 + 0.25\Gamma(E)^2}; \quad \Gamma(E) = \Gamma_R \frac{E^{0.5}}{E_R^{0.5}} \quad (28)$$

where E_R and Γ_R are the energy and width of the populated resonance.

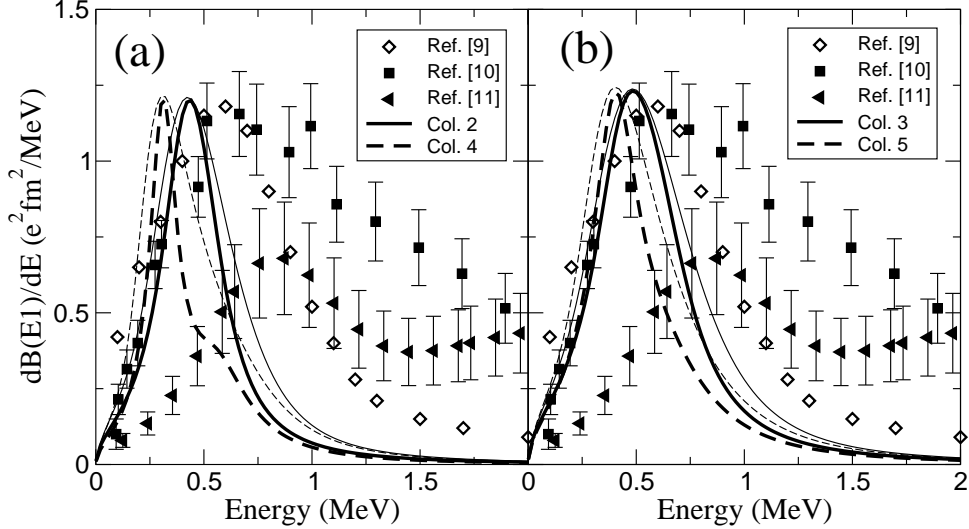


Fig. 5. (a) Differential $B(E1)$ -values obtained with the three-body resonances in columns 2 (solid line) and 4 (dashed line) in table 4. (b) The same as in the right part but for columns 3 (solid line) and 5 (dashed line). In both figures the thin lines are the calculations after convoluting with the response of the detector (see text). Experimental data are from [9], [10], and [11], where the beam energies are 28 MeV/nucleon, 43 MeV/nucleon, and 280 MeV/nucleon, respectively.

In fig.5 we show the differential $B(E1)$ -strength computed as given in eq.(24). The photonuclear cross section σ_{E1} is computed for the four sets of resonance energies in columns 2 to 5 in table 4 as a weighted average of the three Breit-Wigner functions (28) obtained for $J^\pi = 1/2^+$ (weight=1/6), $J^\pi = 3/2^+$ (weight=2/6), and $J^\pi = 5/2^+$ (weight=3/6). The weight of each angular momentum J is dictated by the different number of angular momentum projections in each case. The solid and dashed lines show the results obtained with the resonance energies given in columns 2 and 4 of table 4 (fig.5a), and in columns 3 and 5 (fig.5b), respectively. The thick lines are the calculations as described above, while the thin lines correspond to the transformation given in eq.(27). The detector response function has been taken to be a gaussian whose width fits the experimental width given in [9] (width= $0.402E^{0.633}$ MeV). As seen in the figure, the convolution (27) makes the curves slightly broader than the original ones. The experimental data shown in the figure are taken from [9] (open diamonds) that correspond to a ^{11}Li beam energy of 28 MeV/nucleon, from [10] (black squares) corresponding to a beam energy of 43 MeV/nucleon, and from [11] (black triangles) where the beam energy is 280 MeV/nucleon. The experimental data given by the open diamonds correspond to the differential $B(E1)$ strength obtained in ref.[9] following eqs.(24) and (28) and using the resonance parameters $E_R = 0.7$ MeV and $\Gamma_R = 0.8$ MeV that according to ref.[9] reproduce the experimental decay-energy spectrum. The computed curves are all scaled to the maximum of the experimental data.

As seen in the figure the experimental data do not agree with each other. At least for the sets of data from refs.[9] and [10], for which the ^{11}Li beam energy is similar, one would expect also a similar experimental distribution. More consistent and accurate experimental measurements are therefore necessary. It is also clear from the figure that the computed curves are in obvious disagreement with the experimental data, especially when comparing with the ones in refs.[10] and [11]. However, several important points should be taken into account. First, it is demonstrated in [31] that in the method of complex coordinate rotation the contributions from both two and three-body non-resonant continuum structures are essential to obtain the full strength function. Including only Breit-Wigner shapes around three-body resonances omits most of the sometimes large two-body contribution. Staying on the real energy axis as in [15,19] all contributions are in principle included but of course only at the correct energies if the correct final state continuum wave functions and the correct reaction mechanism are used. Second, the role played by the nuclear projectile–target interactions has not been considered. For low beam energies this contribution is certainly negligible while for beam energies above 200 MeV/nucleon, as the one used in [11], previous calculations for ^{11}Li on Pb show that the nuclear contribution could amount up to 30% of the total two–neutron removal cross section [52]. Finally, the different effect produced by the possible reaction mechanisms has also to be taken into account. Actually the different experiments are analyzed in different ways indicating the belief in a corresponding reaction mechanism. While in [9] the authors assume a decay through resonances, in [10] the experimental data are reproduced assuming a direct breakup mechanism. Other mechanisms, as decay after populating two–body (neutron–core) resonances [31] could also be important.

We can then conclude that not only experimentally, but also from the theoretical point of view, a careful analysis of the reaction process is required. Reproducing the strength function with a model without the decisive features has very little significance. To emphasize this point we compare in fig.6 different calculations of the Coulomb dissociation cross section. Calculations assuming a decay through three–body resonances (eqs.(24) and (28)) are shown by the thick solid line, thick dashed line, and thin solid line, that correspond, respectively, to our calculations using the complex rotation method and using the three–body resonances shown in columns 2 and 4 of table 4, and the calculation using the values of E_R and Γ_R given in [9]. The thin dashed line is the calculation described in [10], that assumes a direct breakup mechanism. This curve matches the experimental data given in the same reference. The two remaining curves are calculations using a full continuum three-body wave function in the real energy axis. The first one (dot–dashed line) is the calculation described in [15]. In this case the spin-3/2 ^{11}Li ground–state wave function is obtained by solving the Faddeev equations by use of the hyperspherical adiabatic method and the final state interactions between the three particles are included. The second one (dotted line) is a calculation similar to

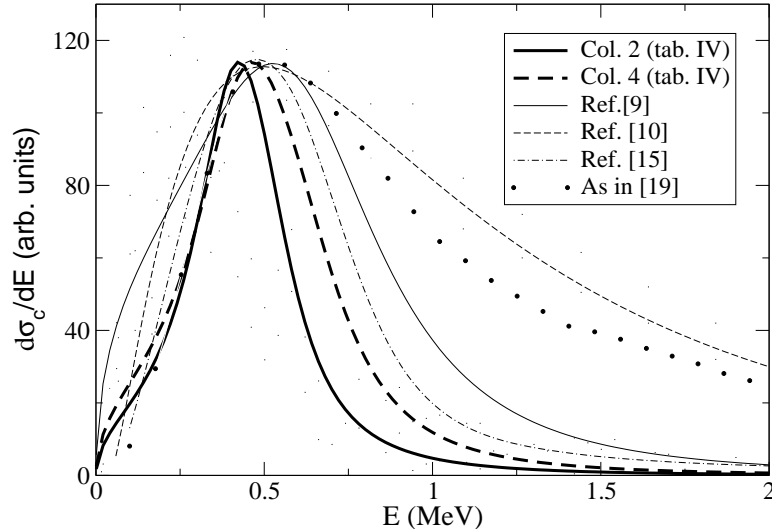


Fig. 6. Differential Coulomb dissociation cross section after fragmentation of ^{11}Li on Pb. The thick solid and thick dashed lines are the calculation as described in the text for the resonances in columns 2 and 4 of table 4. The thin solid line, the thin dashed line, and the thin dot-dashed line are the calculations as described in refs.[9], [10], and [15], respectively. The dotted line is the result of a calculation using spin 0 for the ^{11}Li projectile and no final state interactions. This calculation is similar to the ones shown in [19]. All curves are scaled to the same maximum.

the one in [15] but taking spin zero for the ^{11}Li ground-state wave function and using plane waves in the final state. These are the same conditions as the ones used in [19], and the computed curve is actually similar to the ones shown in this reference.

The pronounced differences between the computations reveals the importance of the inclusion of all the correct ingredients: The right reaction mechanism and the right final state interaction including not only the final three-body continuum structures but also the contribution from two-body continuum states. Proper computations could be like in [31] with the appropriate spin splitting or as in [2] where the dominating decay mechanism proceeds via the low-energy three-body continuum and the final state interaction is incorporated by use of three-body distorted continuum wave functions. Both calculations are rather elaborate and beyond the scope of this paper.

6 Summary and conclusions

The hyperspheric adiabatic expansion has been very successful in descriptions of ground states of three-body halo nuclei and especially for Borromean systems. In addition a series of breakup reaction processes are well described in the same model supplied with appropriately specified reaction mechanisms.

Complex scaling as a tool to compute resonance energies has also been very successful and frequently used especially in atomic and molecular physics. However, the method has also proven efficiency in applications to nuclei, including halo nuclei. Combining these methods of hyperspheric adiabatic expansion and complex rotation therefore seems to be worthwhile.

The smoking gun signal for three-body halos was first found in the reaction cross section of ^{11}Li and subsequently this nucleus has been thoroughly studied. However, amazingly few realistic computations of continuum states exist and in particular of resonances. The reasons for this fact are that such continuum three-body computations are difficult and especially for ^{11}Li due to the finite spin of both the nucleus itself and the ^9Li . Furthermore the two-body interactions are not accessible to direct measurements and consequently not very well established. The present level of accuracy and sophistication demand that all observables are computed consistently within the same model.

These theoretical problems have more or less disappeared during the recent years. The same model has for ^{11}Li been used for essentially all known ground state and three-body breakup observables. A consistent set of interaction parameters is established in agreement with the available experimental data, but not yet applied on continuum properties. We therefore first remove the last obstacle, i.e. formulation of complex scaling in connection with the hyperspheric expansion. An important ingredient is to account for the antisymmetrization between core and valence neutrons. In our model this is achieved by using phase equivalent two-body potentials. Thus we first formulate complex scaling for such potentials in connection with the present method.

After the formalism and model parameters are made available we investigate excitations where a 1^- angular momentum and parity is transferred to the ground state of ^{11}Li . This implies three sets of quantum numbers $J^\pi = 1/2^+$, $3/2^+$ and $5/2^+$ and we search for corresponding resonance states. The lowest adiabatic potentials are only marginally different for the three sets of quantum numbers with attractive pockets at relatively small values of ρ . The radial wave functions are therefore very similar with peaks at small values of ρ indicating resonance properties. The eigenvalues correspondingly reveal low-lying resonance states scattered around the results for zero core spin (zero spin-splitting) of position above threshold and width of (0.48, 0.33) MeV. This corresponds to an excitation energy position of about 0.78 MeV, i.e. a few hundred keV below the results extracted from measurements. The lowest of the spin split resonances would for the most favorable interaction even lie lower at an excitation energy of 0.74 MeV.

The resonance position is off hand low compared to the quoted experimental value. However, other information about Coulomb dissociation cross sections or B(E1)-strength functions is also closely connected to the structure of the

1^- -excitations. Three experiments derive these quantities, but unfortunately all in mutual disagreement. They claim and use different reaction mechanisms in the derivations. One uses a parametrization in terms of three-body resonances in the complex plane. This is insufficient since significant contributions from the background continuum then are not included. This experiment may also have acceptance problems at the important region of small energies. Another experiment seems to assume that the breakup is a direct process where the corresponding analysis results in a much broader distribution. The third experiment at a higher beam energy of 280 MeV/nucleon most probably also receives contributions from nuclear breakup.

To get an indication we have used the computed three-body resonance parameters and obtained the cross section. Although this is rather far from a correct computation we are thereby able to compare the influence of different continuum spectra on the differential cross section. In general our strength functions come out relatively narrow concentrated at low energies. This is entirely consistent with the calculated low-lying 1^- -resonances. Whether it also is consistent with the measurements remains to be seen in comparison with better experimental values and for correct computations, where the proper reaction mechanism is used. Both these enterprises require a substantial effort, but may well be worth doing. In this paper we have presented our predictions of three-body 1^- -resonances in ^{11}Li obtained in a model able to reproduce all ground state properties and essentially all other three-body breakup observables.

Acknowledgements We want to thank Karsten Riisager for continuous discussions.

References

- [1] M.V. Zhukov, B.V. Danilin, D.V. Fedorov, J.M. Bang., I.J. Thompson, and J.S. Vaagen, Phys. Rep. **231**, 151 (1993).
- [2] E. Garrido, D.V. Fedorov, and A.S. Jensen, Nucl. Phys. A **695**, 109 (2001).
- [3] E. Garrido, D.V. Fedorov, and A.S. Jensen, Nucl. Phys. A **700**, 117 (2002).
- [4] F. Ajzenberg-Selove, Nucl. Phys. A **506**, 1 (1989).
- [5] T. Aumann *et al*, Phys. Rev. C **59**, 1252 (1999).
- [6] D. Aleksandrov *et al*, Nucl. Phys. A **669**, 51 (2000).
- [7] S.N. Ershov, T. Rodge, B.V. Danilin, J.S. Vaagen, I.J. Thompson, and F.A. Gareev, Phys. Rev. C **56**, 1483 (1997).

- [8] B.V. Danilin, I.J. Thompson, J.S. Vaagen, and M.V. Zhukov, Nucl. Phys. A **632**, 383 (1998).
- [9] D. Sackett *et al.*, Phys. Rev. C **48**, 118 (1993).
- [10] S. Shimoura, T. Nakamura, M. Ishihara, N. Inabe, T. Kobayashi, T. Kubo, R.H. Siemssen, I. Tanihata, and Y. Watanabe, Phys. Lett. B **348**, 29 (1995).
- [11] Zinser *et al.*, Nucl. Phys. A **619**, 151 (1997).
- [12] A.A. Korshennikov *et al.*, Phys. Rev. C **53**, R537 (1996).
- [13] A.A. Korshennikov *et al.*, Phys. Rev. Lett. **78**, 2317 (1997).
- [14] M.G. Gornov, Y. Gurov, S. Lapushkin, V. Pechkurov, T.K. Pedlar, K.K. Seth, J. Wise, and D. Zhao, Phys. Rev. Lett. **81**, 4325 (1998).
- [15] A. Cobis, D.V. Fedorov and A.S. Jensen, Phys. Rev. C **58**, 1403 (1998).
- [16] S. Kumar and V.S. Bhasin, Phys. Rev. C **65**, 034007 (2002).
- [17] M.V. Andrés and J. Gómez-Camacho, Phys. Rev. Lett. **82**, 1387 (1999).
- [18] A. Bonaccorso and N. Vinh Mau, Nucl. Phys. A **615**, 245 (1997).
- [19] C. Forssén, V.D. Efros, and M.V. Zhukov, preprint nucl-th/0201057.
- [20] J. Aguilar and J.M. Combes, Commun. Math. Phys. **22**, 169 (1971).
- [21] E. Balslev and J.M. Combes, Commun. Math. Phys. **22**, 280 (1971).
- [22] B. Simon, Commun. Math. Phys. **27**, 1 (1972).
- [23] Y.K. Ho, Phys. Rep. **99**, 1 (1983).
- [24] N. Moiseyev, Phys. Rep. **302**, 212 (1998).
- [25] A. Csótó, Phys. Rev. C **49**, 2244 (1994).
- [26] J. Wang, S. Chu, and C. Laughlin, Phys. Rev. C **50**, 3208 (1994).
- [27] A. Csótó, H. Oberhummer, and R. Pichler, Phys. Rev. C **53**, 1589 (1996).
- [28] K. Arai, Y. Ogawa, Y. Suzuki, and K. Varga, Phys. Rev. C **54**, 132 (1996).
- [29] A. Csótó, Phys. Rev. C **49**, 3035 (1994).
- [30] S. Aoyama, S. Mukai, K. Kato, and K. Ikeda, Prog. Theor. Phys. **94**, 343 (1995).
- [31] T. Myo, K. Kato, S. Aoyama, and K. Ikeda, Phys. Rev. C **63**, 054313 (2001).
- [32] S. Aoyama, K. Kato, and K. Ikeda, Phys. Rev. C **55**, 2379 (1997).
- [33] S. Aoyama, K. Kato, T. Myo, and K. Ikeda, Prog. Theor. Phys. **107**, 543 (2002).
- [34] E. Garrido, D.V. Fedorov, and A.S. Jensen, Phys. Rev. C **99**, 1272 (1999).
- [35] D.V. Fedorov and A.S. Jensen, Phys. Rev. Lett. **71**, 4103 (1993).

- [36] D.V. Fedorov, A.S. Jensen, and K. Riisager, *Phys. Rev. C* **50**, 2372 (1994).
- [37] E. Nielsen, D.V. Fedorov, A.S. Jensen, and E. Garrido, *Phys. Rep.* **347**, 373 (2001).
- [38] D.V. Fedorov, E. Garrido, and A.S. Jensen, *Phys. Rev. C* **51**, 3052 (1995).
- [39] E. Garrido, D.V. Fedorov, and A.S. Jensen, *Europhys. Lett.* **43**, 386 (1998).
- [40] D.V. Fedorov, A.S. Jensen, and E. Garrido, to be published.
- [41] N. Moiseyev, P.R. Certain, and F. Weinhold, *Molec. Phys.* **36**, 1613 (1978).
- [42] E. Garrido, D.V. Fedorov, and A.S. Jensen, *Nucl. Phys. A* **650**, 247 (1999).
- [43] C.V. Sukumar, *J. Phys. A* **18**, 2937 (1985).
- [44] D. Baye, *Phys. Rev. Lett.* **58**, 2738 (1987).
- [45] H. Fiedeldey, S.A. Sofianos, and A. Papastylanos, K. Amos, and L.J. Allen, *Phys. Rev. C* **42**, 411 (1990).
- [46] D. Baye, *J. Phys. A* **20**, 5529 (1987).
- [47] H.G. Bohlen, W. von Oertzen, Th. Stolla, R. Kalpakchieva, B. Gebauer, M. Wilpert, Th. Wilpert, A.N. Ostrowsky, S.M. Grimes, and M.N. Massey, *Nucl. Phys. A* **616**, 254c (1997).
- [48] E. Garrido, D.V. Fedorov, and A.S. Jensen, *Nucl. Phys. A* **617**, 153 (1997).
- [49] F. Ajzenberg-Selove, *Nucl. Phys. A* **490**, 1 (1988).
- [50] J. Carlson and R. Schiavilla, *Rev. Mod. Phys.* **70**, 743 (1998).
- [51] C.A. Bertulani and G. Baur, *Phys. Rep.* **163**, 299 (1988).
- [52] E. Garrido, D.V. Fedorov, and A.S. Jensen, *Europhys. Lett.* **50**, 735 (2000).